Silicon photonic microelectromechanical systems add-drop ring resonator in a foundry process

Hamed Sattari[a],[*],[†] Alain Yuji Takabayashi,[a],[‡] Pierre Edinger[b], Peter Verheyen,[c] Kristinn B. Gylfason[b], Wim Bogaerts[d,e] and Niels Quack[a,f,§]

[a]École Polytechnique Fédérale de Lausanne, Lausanne, Switzerland
[b]KTH Royal Institute of Technology, School of Electrical Engineering and Computer Science, Division of Micro and Nanosystems, Stockholm, Sweden
[c]Interuniversity Microelectronics Centre, Leuven, Belgium
[d]Ghent University, Ghent, Belgium
[e]Center for Nano- and Biophotonics (NB Photonics), Ghent, Belgium
[f]The University of Sydney, School of Aerospace, Mechanical and Mechatronic Engineering, Sydney, New South Wales, Australia

Abstract Photonic add-drop filters are crucial components for the implementation of wavelength division multiplexing (WDM) in fiber-optic communication systems. The recent progress in photonic integration has shown the potential to integrate photonic add-drop filters alongside high-performance photonic building blocks on a chip to construct compact and complex photonic-integrated circuits for WDM. Typically, implementations are based on micro-ring resonators with integrated heaters or free carrier dispersion-based modulators to adjust the filter wavelength. However, heaters suffer from high power consumption, and free carriers result in optical absorption losses, limiting the scalability toward very-large-scale circuits. We demonstrate the design, simulation, fabrication, and experimental characterization of a compact add-drop filter based on a vertically movable, MEMS-actuated ring resonator. The MEMS-actuated add-drop filter is implemented in IMEC's iSiPP50G silicon photonics platform and realized using a short post-processing flow to safely release the suspended MEMS structures in a wafer-level compatible process. The filter exhibits a through port linewidth of ∼1 nm (124.37 GHz) at 1557.1 nm, and it retains a port extinction of 20 dB and a port isolation of >50 dB under 27 V of actuation voltage. The combination of low-power consumption and a compact footprint demonstrates the suitability for very-large-scale integration in photonic circuits. © *The Authors. Published by SPIE under a Creative Commons Attribution 4.0 International License. Distribution or reproduction of this work in whole or in part requires full attribution of the original publication, including its DOI.* [DOI: 10.1117/1.JOM.2.4.044001]

1 Introduction

Add-drop filters play a crucial role in optical wave routing and processing in photonic integrated circuits (PICs) for a variety of applications. An efficient type of this filter is the micro-ring resonator, which enables precise and efficient spectral manipulation due to its resonant nature, resulting in a narrow-band filter response and high extinction ratio. These optical properties

---

*Address all correspondence to Hamed Sattari, hamed.sattari@csem.ch

[†]Present address: H. Sattari (hamed.sattari@csem.ch) is currently with Swiss Center for Electronics and Microtechnology (CSEM), CH-2002 Neuchâtel, Switzerland.

[‡]Present address: A. Y. Takabayashi is now with Enlightra, Switzerland.

[§]Present address: N. Quack is currently with The University of Sydney, Australia. The work reported in this manuscript was performed while N. Quack was at EPFL (affiliation a), and the manuscript was partially composed while N. Quack was at the University of Sydney (affiliation f).

become more attractive when connecting several micro-ring resonators in a cascade to perform advanced signal routing and spectrum engineering for telecommunication applications.[1] Consequently, the implementation of micro-ring resonator circuits in PICs has proven to be an efficient method for integrated wavelength division multiplexing (WDM), which makes it possible to increase data traffic density in a physical telecommunication channel.[2,3] Circuits with increased complexity, e.g., in dense WDM (DWDM) systems, require large-scale integration of wavelength add-drop filters on chip,[4] imposing constraints on the power consumption and optical performance of every individual filter, and they should also have a compact footprint to accommodate numerous components on a single chip.

Among the various integrated photonic platforms that have successfully implemented micro-ring resonator-based add-drop filters for WDM applications, silicon photonics is acknowledged as a prominent platform. Its material system, design flow, manufacturing processes, and technology infrastructure build heavily on those of the complementary metal-oxide-semiconductor (CMOS) electronics technology, thereby providing a significant advantage in terms of future volume manufacturing and economy of scale. Additionally, the large refractive index contrast in silicon photonic waveguides allows for waveguides with small bending radii below 5 μm, so devices can be made very compact. Several established silicon photonics platforms already offer large libraries of standard components to fabless PIC designers. In the past decade, the foundries offering these services have expanded their libraries by adding new devices and designs to address the emerging needs in application areas that include high-performance computing, telecom/datacom, and optical sensing.[5]

A key component in silicon photonic circuits is the micro-ring resonator. Due to the compact silicon waveguides, this resonant filter component can be very compact, making it useful for filters that span a large free spectral range (FSR). Current actively controlled silicon photonic micro-ring resonator add-drop filters are based on either the thermo-optic coefficient of silicon waveguides or the carrier concentrations in the active region of the waveguides. Various designs have been exploited to optimize the performance of these components. Thermally controlled add-drop filters can offer a wide range of tunability (>10 nm) and are of great interest for applications requiring optical spectrum manipulation over a broad spectral range, such as for hybrid tunable lasers.[6,7] However, two main drawbacks of this type of filter are its relatively slow response time and its high-power consumption. Furthermore, parasitic thermal crosstalk limits the spacing between components and, therefore, the number that can be integrated in a single circuit.[8] Alternatively, add-drop filters based on the plasma dispersion effect (i.e., carrier concentration) offer a fast switching time in the nanoseconds range and do not suffer from substantial crosstalk.[9,10] However, these filters typically offer a limited tuning range and exhibit excessive optical losses due to photon-carrier scattering in the active region of the component. Although PIC foundries are striving to further optimize the performance of the thermo-optic and carrier-injection filters and modulators, in parallel, there have been several efforts underway suggesting solutions such as incorporating plasmonic components, liquid crystals, phase-change materials, etc. into the PIC platforms to deliver efficient phase shifters, switches, and filters.[11–13] Although such developments broaden the application scope of the PICs, they are still deficient to provide sufficiently compact, low loss, and fast building blocks compatible with a foundry process.

Photonic microelectromechanical systems (MEMS) offer a low-power and potentially low-loss and compact alternative to these existing standard building blocks for silicon photonics and satisfy the criteria for large-scale integration needed in the telecommunication domain and the emerging fields of neuromorphic computing, quantum processing, and programmable photonics.[14] In particular, the photonic MEMS-based approach benefits from the physical movement of waveguides, which can be achieved using electrostatic actuation, thereby enabling large effective index tunability with low-power operation.[14–17] Moreover, integration of photonic MEMS into standard silicon photonic platforms is a natural next step in technology integration, as silicon is one of the most used materials for MEMS technology. In recent years, various MEMS micro-ring resonator add-drop filters have been realized based in silicon.[18–21] In these demonstrations, the amplitude of the add/drop signals or the rings' FSR are tuned by moving the waveguides (either bus or the resonator) to effectuate a change in either the effective index of the resonant mode or the coupling coefficient between the bus waveguide and the resonator.

We present the detailed simulation flow and analysis of a MEMS-tunable add-drop filter for add/drop signal amplitude switching and a critical discussion on the experimental measurement results. Our photonic MEMS component is integrated in the full stack of the iSiPP50G standard platform[22] along with library-standard components.[23] The procedure by which the MEMS devices are made free-standing requires a few post-processing steps and can be performed at the wafer level. Our approach, corroborated by the promising performance of the device, suggests that the libraries of standard silicon photonic platforms would benefit from the addition of photonic MEMS-based components because of their compact size and low tuning power.

2 Working Principle and Design

Our MEMS add-drop filter follows a conventional racetrack micro-ring resonator architecture in which a micro-ring resonator is coupled to two bus waveguides, resulting in four ports. The substantial difference from standard designs is the inclusion of the physical mechanism that is used to tune the waveguide gaps in the coupled regions and modify the amplitudes of the add/drop signals. A schematic representation of the presented silicon photonic MEMS add-drop filter and its scaled layout are shown in Fig. 1.

The filter consists of one suspended, vertically movable micro-ring resonator and two suspended waveguides coupled to the ring from two sides. The movable micro-ring resonator follows a racetrack design and consists of two fully etched wire waveguides in the coupling regions, two rib waveguides in the anchoring regions, four tapered waveguide transitions connecting the wire waveguides to the rib waveguides, and four bent wire waveguides. This design enables a few crucial functionalities. First, the suspended wire waveguides in the coupling regions facilitate efficient coupling between the bus waveguide and the ring within a short length of 10 μm. When the ring is vertically aligned to the bus waveguides, we simulated 30% power coupling for a single directional coupler, which makes the couplers the dominant loss mechanism in the ring, providing a high transmission to the drop port. Second, the straight rib waveguide sections connected to the anchors at a safe distance from the rib core enable low-loss wave propagation while providing the structural rigidity needed to keep the ring stable during actuation. And third, the tapered waveguide transitions are designed to transfer the light between the two waveguide types smoothly without increasing the device footprint. This micro-ring resonator is anchored from the rib waveguide sections to a pair of parallel plate electrostatic actuators that provide vertical displacement. The suspended bus waveguides are anchored by waveguide transitions that have been designed to allow light to pass from the oxide-clad region of the chip into the air-clad region (MEMS cavity) with low loss.[23,24] Furthermore, these anchors are designed to limit the etching within the MEMS box region and prevent an attack of the back-end-of-line (BEOL) stack. A detailed discussion of the anchor design is presented in Ref. 24. By applying a voltage between the device layer and substrate (i.e., via the parallel plate actuators), the ring is pulled down. Consequently, the separation between the suspended waveguides and the micro-ring resonator increases, which decreases the coupling to and from the ring and modifies the fraction of power
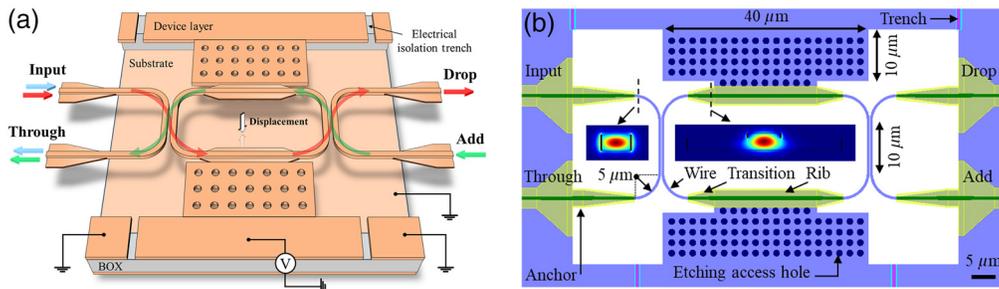

Fig. 1 (a) Schematic representation of the MEMS add-drop filter (not to scale). The device is tuned by actuating the vertically movable suspended ring resonator and (b) layout of the device with the scaled dimensions. Optical mode profile in the fully etched and shallow etched waveguide sections are shown in the inset. No color code relation is applied between the two figures.

transmitted to the drop and through ports. Hereafter, we use the terms Filter-ON and Filter-OFF states, for the passive (no bias) state and the active (actuated) state of the device, respectively. In the Filter-OFF state, the coupling to the ring is almost zero, and the light propagates from the input to the through port with a very low extinction at the resonances.

The two suspended directional couplers are 10-μm long, and the bent waveguides have a bend radius of 5 μm. The waveguide widths are 450 and 650 nm for the fully etched and shallow-etched waveguide regions, respectively, and the airgap between the coupling waveguides and micro-ring resonator is 150 nm in the unactuated state. As defined by the iSiPP50G standard process, the final waveguide height is expected to be 214 nm, and the shallow waveguide section has a ridge height of 70 nm. At 45 μm $\times$ 75 μm, this device has a small footprint, which is advantageous for large-scale integration. The device has four ports, which we label input, through, add, and drop. From an operational perspective, the optical carrier enters the circuit from the input port, couples to the resonator through the first coupler, and circulates in the MEMS ring resonator before coupling through the second directional coupler and transferring to the drop port. There is also light coupling out through the first directional coupler, and at resonance this interferes destructively with the original wave and suppresses the transmission in the through port.[9] To add a wavelength to the spectrum, an additional optical carrier at the resonance wavelength can be launched from the add port and is transferred to the through port after circulating in the resonator. Based on the design, the MEMS ring resonator supports filtering of carrier wavelengths in the telecommunication C-band with an FSR of 5.28 nm. The dimensions shown in Fig. 1(b) are the result of a mechanical and optical design optimization process of determining a geometry providing low-loss and efficient optical performance for an acceptable range of applied voltages, as well as minimizing the potential mechanical failure modes such as a post-release suspended waveguide deformation in the passive state and asymmetric mechanical displacement and the collapse upon actuation. To calculate the FSR of the micro-ring resonator, we follow the conventional analytical formula for micro-ring resonators:

$$\text{FSR} = \frac{\lambda^2}{n_g L}, \tag{1}$$

where λ, n_g, and L are the wavelength, group index, and round-trip length, respectively. It is worth noting that, in our case, the group index varies between different sections of the ring. Therefore, to approximate the FSR, we need to obtain the group index in each section, multiply it by the corresponding length of that section, and finally sum all products to obtain the term in the denominator of Eq. (1). Thus, the FSR of the MEMS micro-ring resonator equals

$$\text{FSR} = \frac{\lambda^2}{n_w L_w + n_r L_r + n_b L_b + n_t L_t}, \tag{2}$$

with subscripts w, r, b, and t indicating wire, rib, bend, and taper, respectively. We approximate the group index of the tapered waveguide transitions (n_t) by a piecewise linear approximation of the group index along the taper (5 μm), calculating the group index in six cross-sections at 1 μm steps as the cross-section geometry evolves along the taper. The extraction of the group index in any desired waveguide cross-section is done through a two-dimensional finite difference eigenmode simulation. From these simulations, we obtain $n_w = 4.5272$, $n_r = 3.7035$, $n_b = 4.5158$, and $n_t = 3.7073$ and, thus, an estimate an FSR of ~5.28 nm at $\lambda = 1550$ nm.

3 Simulation Results

Optical domain simulations of the device are performed using finite-difference time-domain (FDTD) models, and the electromechanical behavior is simulated using finite element method (FEM) software. In the first set of optical simulations, the group indices in the waveguide section are extracted to calculate the FSR using Eq. (2). Next, a light propagation simulation in the Filter-ON state (i.e., the ring sheds optical power much faster through both couplers than through other internal loss mechanisms) is performed, and this provides a simulated FSR of ~5.1 nm that is consistent with the value of 5.28 nm obtained from the semi-analytical calculation.
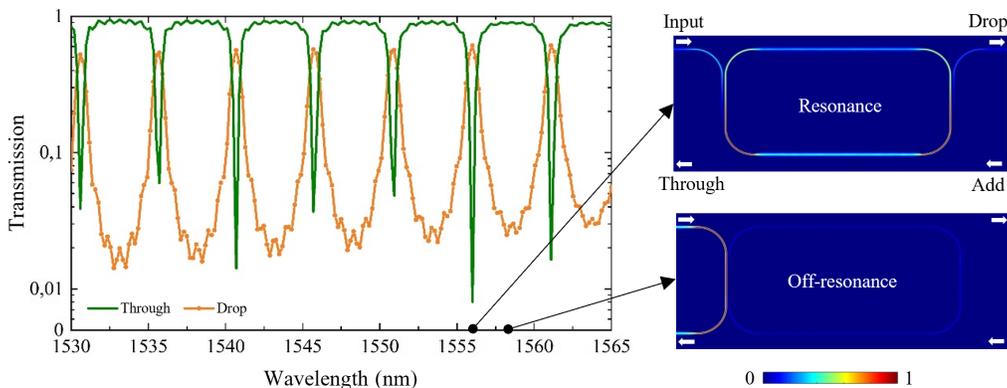
Fig. 2 Transmission spectra of add and drop ports of the MEMS filter obtained from 3D FDTD simulation in the Filter-ON state (passive state). At the right, optical power profiles are shown for the resonant and off-resonant wavelengths.

In the electromechanical simulation, the bias voltage is swept, and the vertical displacement of the ring toward the substrate is recorded. In this manner, an actuation curve characterizing the voltage-dependent vertical displacement of the coupled waveguide section of the micro-ring resonator is generated. This actuation curve identifies the voltage required for the Filter-OFF state of the device. In particular, a noticeable reduction in transmitted power to the drop port is expected as soon as the coupling between the micro-ring resonator and the bus waveguides decreases through out-of-plane misalignment of the bus waveguides to the micro-ring resonator. In parallel, a mechanical eigenfrequency simulation is performed to extract the mechanical eigenmodes of the device, which is discussed further at the end of this section.

The optical simulation results are shown in Fig. 2, where the transmission spectra at the add and drop ports as well as the optical power profile in the Filter-ON state for the resonant and off-resonant wavelengths are presented. It is worth noting that, due to the resonant nature of the structure, performing a full three-dimensional (3D) FDTD simulation of the device is not time or memory efficient. Therefore, the simulation is truncated, and this leads to some uncertainty in defining the extinction ratios and the resonance bandwidth. However, it is still evident that, in the Filter-ON state (passive), light at the resonant wavelength is efficiently transferred from the input port to the drop port. O the other hand, most of the optical power of off-resonance wavelength light propagates into the through port, as shown in Fig. 2. To reduce the power in the drop port, the coupled waveguides must be misaligned with respect to the micro-ring resonator by vertical displacement. Optical simulations indicate that 500 nm of vertical displacement is sufficient for placing the device in the Filter-OFF state. This amount of vertical displacement lies safely within one third of the gap between the device layer and substrate (2 μm) and, thus, guarantees device operation within a safe margin of the well-known vertical pull-in failure regime for vertically-actuated electrostatic MEMS.[25] We define the Filter-OFF state at a vertical displacement of 500 nm, where we observe no power coupling; however, it is important to note that the transmitted power already drops very rapidly as soon as the coupling decreases between the micro-ring resonator and the waveguides, which already occurs at smaller vertical displacements.

Figure 3(a) shows the electromechanical simulation results in which the absolute value of the vertical displacement of a selected probe point on the micro-ring resonator (Δz) is plotted against the applied bias between the electrode pair and the substrate. The curve follows a parabolic path, as expected from the parallel plate actuator scheme.[25] The misalignment between the micro-ring resonator waveguide and the bus waveguides reaches 350 nm (vicinity of the filter-off state) at 30 V of bias voltage.

The color-coded inset of Fig. 3(a) shows the vertical displacement of the micro-ring resonator for an actuation voltage of 30 V. The vertical displacement for the coupler waveguide exceeds the displacement of the electrode plates owing to the higher stiffness of the electrode plates. Note that, because the ring resonator is vertically displaced, it also slightly deforms as the rib waveguide sections are pulled outward. From our simulations (not shown in Fig. 3), the maximum amplitude of such an in-plane deformation remains below 8 nm at 30 V of the actuation voltage.
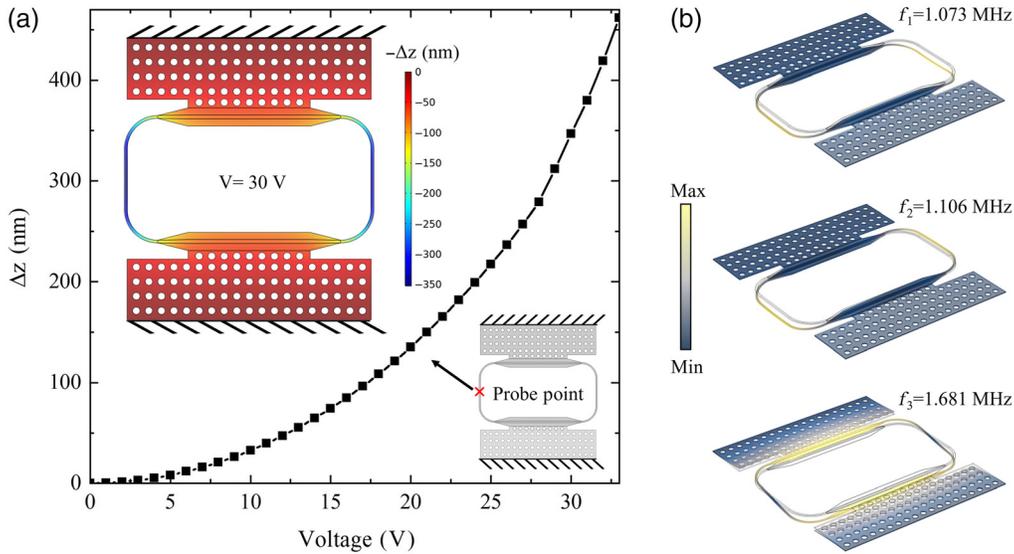
Fig. 3 (a) Electromechanical simulation results showing the actuation curve of the micro-ring resonator. The vertical displacement of the ring for $V = 30$ V is demonstrated in the inset. (b) Three first eigenfrequencies of the MEMS micro-ring resonator.

The mechanical eigenmode simulation results are shown in Fig. 3(b), where the first three modes of the device are plotted. It is important that the fundamental mechanical mode of the device supports a stable vertical movement of the ring with symmetrically displaced coupled waveguide arms. The fundamental mode follows the desired stable configuration with an eigenfrequency of 1.073 MHz, indicating a switching speed in the microseconds range. Although in this work we are focused on a translational displacement coinciding with the fundamental mode profile of the device, the two succeeding tilting modes would also be of interest for the device operation because a device deformation with those mode profiles can contribute to a drastic misalignment between the coupled waveguides, which consequently switches the filter.

4 Fabrication Process

To realize the photonic MEMS filter, we follow the design rules of the iSiPP50G process at IMEC through the provided process design kit.[26] Due to an existing foundry process module for opening the BEOL dielectric stack down to a thin oxide layer above the waveguide layer, it is possible to access the silicon device layer in specific regions of the chip where the MEMS devices are located. These openings are essential for enabling the subsequent release process. It is important to note that the photonic MEMS devices are integrated alongside various standard components, such as heaters, electro-optical modulators, and photodetectors, and the wafer contains the full stack available in the platform, enabling all of the iSiPP50G functionality.[27] The 200-mm wafer from the foundry are diced into 46 mm × 46 mm coupons that undergo a set of subsequent post-processing steps performed at the EPFL Center of Micronanotechnology to release the MEMS devices by selectively removing the buried oxide (BOX) layer underneath them and making them free-standing and movable. The main steps of this post-processing flow for the photonic MEMS release are shown in Fig. 4.

In the first preparation step, the thin remaining oxide on top and between the waveguides is removed by a dedicated lithography and buffered hydrofluoric acid etch, which results in the cross section of Fig. 4(a). The main goal of the post-processing is to locally release the MEMS device from the 2-μm BOX underneath the silicon device layer. A safe release process should not affect the other devices on the chip and, thus, requires a protection layer against the vapor-phase hydrofluoric acid (VHF) etchant used to remove this BOX. Failure to do so could result in device malfunctioning and/or structural failure of the cavities due to the etchant attack on the BEOL. Therefore, the next step in the post-processing sequence is the deposition of a 50-nm thick
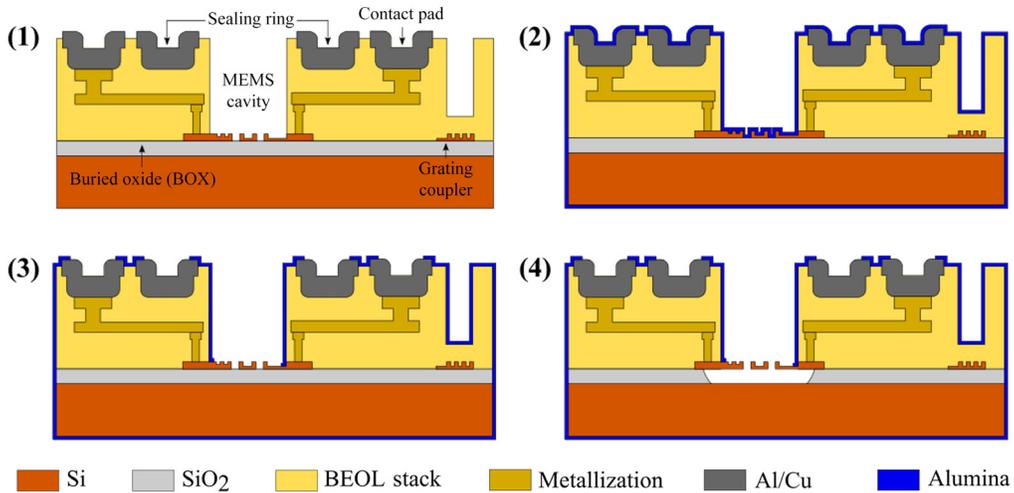
Fig. 4 Post-processing steps for releasing the silicon photonic MEMS components: (1) starting stack after preparatory removal of the remaining oxide on and between the waveguides, (2) alumina passivation by ALD, (3) alumina patterning by dry/wet etching, and (4) VHF release etch to remove the BOX.

conformal alumina passivation using atomic layer deposition (ALD). Next, access windows within the MEMS cavities are defined by maskless lithography and selective etching of the alumina by a combination of dry and wet etching processes. In the final MEMS release step, the 2-μm BOX underneath the device layer is selectively removed by the VHF, which leads to suspended, movable structures.

Figure 5(a) shows an optical microscope image of the chip just after the MEMS release process. The device inside the MEMS cavity is cleanly released, and there is no damage from the release process to neighboring components. Four grating couplers connected to the device provide optical I/O. The optical connection waveguides, the two metallization layers, and the contact pads for electrical I/O are also visible in the image. There is also a sealing ring around the MEMS cavity region that can be used for subsequent hermetic sealing of the device for environmental encapsulation, but that is not used in this work.[28] A closer view of the MEMS cavity is shown in Fig. 5(b), which reveals more detail of the passivation layer opening and the VHF etch front profile.
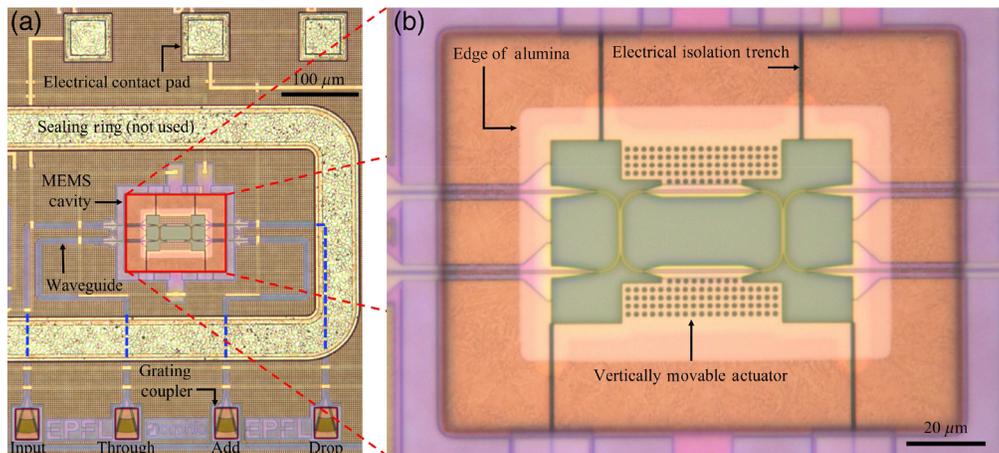

Fig. 5 Optical microscope image of the chip area after vapor phase hydrofluoric acid MEMS release. (a) Successful integration of the MEMS device in the full stack of iSiPP50G platform next to the grating couplers and the electrical bond pads. (b) Closer view of the released MEMS micro-ring resonator filter.
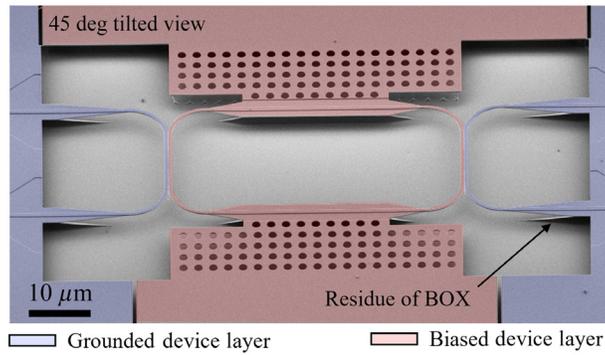
Fig. 6 SEM image of the add-drop filter (false-colored), showing well defined suspended actuators and waveguides.

In Fig. 6, a scanning electron microscope (SEM) image of the MEMS add-drop filter demonstrates the compatibility of the MEMS release process with the standard silicon photonics platform, yielding well-defined suspended actuators and well-aligned and parallel directional coupler waveguides. Although some residues of the BOX from the release step remains on the substrate, the substrate surface is mostly clean of the BOX layer; therefore, we do not expect any parasitic effect to arise from these residues. In case of an uncomplete release step with a residual BOX layer covering the substrate, electrical charges could accumulate locally in the residual layer and originate malfunctions such as actuation voltage drift, hysteresis phenomenon, and decreased pull-in threshold.

5 Characterization and Discussion

Figure 7 shows a schematic diagram of the characterization setup. An array of single-mode fibers connects the tunable laser, photonic chip, and power sensors to one another. The optical signal couples into/out of the chip by means of library-standard vertical grating couplers, and the received power is actively monitored to determine the device transmission at each port. To enable a precise alignment between the fiber array and the grating couplers, the chip is mounted on a three degree-of-freedom (DOF) stage and the fiber array positioning is controlled by a six DOF stage. Actuation of the device and its proper grounding are performed using a set of electrical probes on micro-positioners. A portion of the device layer that encompasses the movable ring resonator is electrified through a metallization path and the related electrical contact pad by a
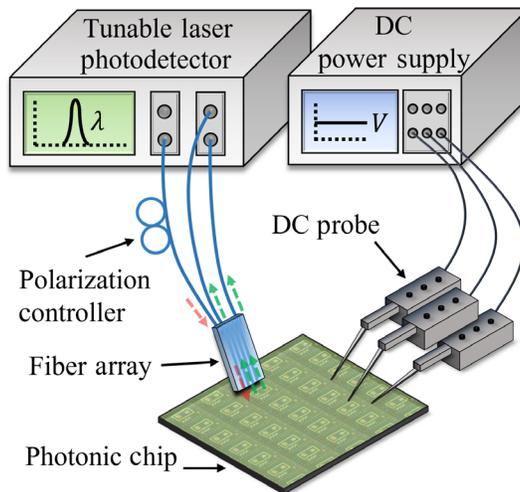

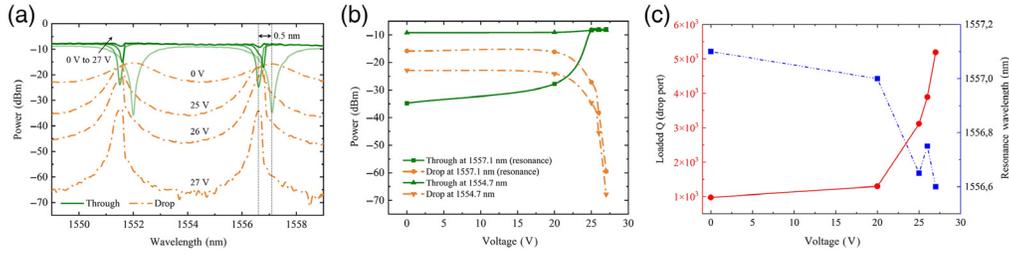**Fig. 7** Schematic of the characterization setup.

Fig. 8 (a) Power spectra of the drop and through ports of the MEMS add-drop filter. (b) Actuation curve of the device at $\lambda = 1557.1$ nm (on-resonance) and $\lambda = 1554.7$ nm (off-resonance). (c) Resonance wavelength shift and the loaded Q factor (drop port) versus the actuation voltage.

direct current (DC) probe tip [see Fig. 5(a)] while the rest of the device layer and the substrate are grounded by two other probe tips through the corresponding contact pads [see Fig. 1(a)].

The drop and through ports' transmission spectra for the Filter-ON (0 V bias) state and a few active (biased) states are shown in Fig. 8(a). The MEMS ring resonator exhibits ~5.1 nm of FSR at the Filter-ON state, which precisely matches optical simulation and analytical calculations. In this state, we observe a through port extinction of ~25 dB at a resonance wavelength of $\lambda = 1557.1$ nm, with a line width of ~1 nm (124.37 GHz) and loaded quality factor Q of 1557.1. In the Filter-OFF state (ultimate active state), with a bias of 27 V, almost all of the optical signal is transferred to the through port and a port isolation of >50 dB is maintained. The required bias voltage falls within the expected voltage range from FEM simulation. Upon actuation, we observe a resonance shift of 0.5 nm [see shown in Fig. 8(c)], or ~10% of the FSR, which corresponds to an induced phase shift of ~0.2π. The origin of this phase shift can be attributed to a combination of effects, including a change in the optical path in the ring resonator upon actuation due to the ring's deformation or a thermally induced wavelength shift due to partial absorption of the optical power in the resonator, The observation of the presence of thermal effects is further evidenced by observation of asymmetry in the resonances shown in Fig. 8(a), which are a typical signature of thermal nonlinearities in ring resonators.[9,29,30] Although initial thermal finite element simulation indicates a clear and expected enhancement of thermal effects due to the removal of the BOX compared with oxide-clad waveguides, the low optical probing power of 1 mW and the modest quality factors appear to not fully account for the phase shift by thermal nonlinearity only, and we expect an additional contribution due to the waveguide deformation upon actuation. Assuming a resonance shift purely due to the micro-ring resonator's deformation and neglecting the group index and the FSR change upon the deformation for the resonance wavelength of 1557.1 nm, we can obtain $\Delta L/L = 0.00064$, which leads to ~70 nm of micro-ring resonator's elongation in the Filter-OFF state. To further assess the contributions to the thermal nonlinearities, further dedicated simulations and experiments are required.

The resonance shift contributes to the large port isolation of >50 dB. From Fig. 8, it can be inferred that, in the case of an ideal zero resonance shift, we would expect a port isolation of ~25 dB, which would be still a promising number. Furthermore, upon actuation from the Filter-ON state to the Filter-OFF state, we observe a progressive linewidth narrowing from 1.6 nm to 0.3 nm at the drop port, as quantitatively shown in the experimentally observed loaded Q factor versus actuation voltage plot in Fig. 8(c). This linewidth narrowing can be understood by a progressive reduction in the light coupling to the micro-ring resonator upon actuation.

The characterization results [Fig. 8(a)] for the drop port in the Filter-ON state at resonance wavelengths indicate an overall device insertion loss of ~7 dB in comparison with the through port transmission in the Filter-OFF state. The experimentally observed loss is significantly higher than the insertion loss of ~1.5 dB predicted by simulation (by a truncated simulation) and can be attributed to a combination of several phenomena: lossy coupling regions, low-quality micro-ring resonator, and asymmetrically coupled micro-ring resonator to the bus waveguides, despite the device not being intentionally designed as such. First, a high insertion loss with a wide drop port linewidth in the Filter-ON state could be mainly related to the coupling losses that take place in the coupled waveguides regions. These losses could originate from fabrication defects and side wall roughness and point connections (footing) in the narrow gaps

(150 nm), which scatter the light in these regions and lead to a loss in both drop and through ports. The amount of the loss in the drop port is expected to be higher in comparison with the through port, as the light transferred to the drop port interacts with two coupling regions, whereas the light traveling to the through port interacts only with one coupling region. Along with the lossy coupling regions, the micro-ring resonator encompasses four waveguide transitions that contribute to a resonator loss and reduce the micro-ring resonator's loaded quality factor to 1557.1, which consequently results in a high loss in the drop port. From Fig. 8(c), it is apparent that, by reducing the coupling to the micro-ring resonator upon actuation, the loaded Q increases as a result of a decreased coupling loss in the drop port side. Finally, the balance between the coupling ratios could be distorted due to a small tilt of the micro-ring resonator upon actuation or fabrication defects leaving the symmetric coupling condition elusive. Finally, we observe a background loss level of ~8 dB, which is attributed to the pair of grating couplers used for optical I/O. From this, we estimate a through port off-resonance insertion loss below 1 dB in the Filter-OFF state. A precise determination of the insertion loss requires dedicated test structures, such as a sequence of couplers; however, these have not been included in the current study.

The actuation curves for selected on-resonance ($\lambda = 1557.1$ nm) and off-resonance ($\lambda = 1554.7$ nm) wavelengths are plotted in Fig. 8(b) (data points are connected by the Bézier function), confirming high port isolation of ~50 and 57 dB for the on- and off-resonance wavelengths, respectively. The device was actuated in multiple cycles (~50×) and showed no hysteresis effect. We also observed a pull-in failure of the actuator at voltages above 34 V. Having the Filter-OFF state bias voltage and the dimensions of the device and assuming a parallel plate capacitor model for the device, we estimate a static power consumption of <50 nW for the demonstrated MEMS add-drop filter, which is substantially lower than the power consumption level of the conventional silicon photonic filters that consume few milliwatts.[18]

6 Conclusion

We report the design, simulation, fabrication, and experimental characterization of a low-power compact MEMS-enabled add-drop filter implemented within IMEC's iSiPP50G standard Silicon Photonics enhanced by custom MEMS release post-processing. The device consists of an electrostatically actuated, vertically moving ring resonator with an FSR of 5.1 nm. The through port extinction of ~25 dB and a port isolation of ~20 dB in the passive state (Filter-ON) of the device and a port isolation of >50 dB for the active state (Filter-OFF) of the device are reported. The characterization results match well with the analytical calculation, as well as FDTD and FEM simulations. The filter retains a line width of 1 nm (124.37 GHz) at 1557.1 nm, which falls in vicinity of the linewidth requirement in WDM systems. The device is actuated with a voltage below 27 V. With a further improvement in the optical design of the device to reduce its insertion loss and resonance linewidth, retaining a compact footprint of 45 μm × 75 μm, with a remarkably low-power consumption, this add-drop filter can serve as an advantageous building block for large-scale DWDM PICs.

References

1. D. G. Rabus and C. Sada, *Integrated Ring Resonators: A Compendium*, Vol. **127**, Springer International Publishing, Cham (2020).
2. P. Dong et al., "Ten-channel discrete multi-tone modulation using silicon microring modulator array," in *Opt. Fiber Commun. Conf.*, Anaheim, California, p. W4J.4 (2016).
3. Q. Xu et al., "Cascaded silicon micro-ring modulators for WDM optical interconnection," *Opt. Express* **14**(20), 9431–9436 (2006).

4. P. Dong, "Silicon photonic integrated circuits for wavelength-division multiplexing applications," *IEEE J. Sel. Top. Quantum Electron.* **22**(6), 370–378 (2016).
5. A. E.-J. Lim et al., "Review of silicon photonics foundry efforts," *IEEE J. Sel. Top. Quantum Electron.* **20**(4), 405–416 (2014).
6. M. A. Tran et al., "Ring-resonator based widely-tunable narrow-linewidth Si/InP integrated lasers," *IEEE J. Sel. Top. Quantum Electron.* **26**(2), 1–14 (2020).
7. S. Srinivasan et al., "Coupled-ring-resonator-mirror-based heterogeneous III–V silicon tunable laser," *IEEE Photonics J.* **7**(3), 1–8 (2015).
8. C. T. DeRose et al., "Thermal crosstalk limits for silicon photonic DWDM interconnects," in *Opt. Interconnects Conf.*, pp. 125–126 (2014).
9. W. Bogaerts et al., "Silicon microring resonators," *Laser Photonics Rev.* **6**(1), 47–73 (2012).
10. G. Li et al., "Ring resonator modulators in silicon for interchip photonic links," *IEEE J. Sel. Top. Quantum Electron.* **19**(6), 95–113 (2013).
11. C. Haffner et al., "Low-loss plasmon-assisted electro-optic modulator," *Nature* **556**(7702), 483–486 (2018).
12. Y. Xing et al., "Digitally controlled phase shifter using an SOI slot waveguide with liquid crystal infiltration," *IEEE Photonics Technol. Lett.* **27**(12), 1269–1272 (2015).
13. M. Delaney et al., "Nonvolatile programmable silicon photonics using an ultralow-loss Sb$_2$Se$_3$ phase change material," *Sci. Adv.* **7**(25), eabg3500.
14. C. Errando-Herranz et al., "MEMS for photonic integrated circuits," *IEEE J. Sel. Top. Quantum Electron.* **26**(2), 1–16 (2020).
15. P. Edinger et al., "Silicon photonic microelectromechanical phase shifters for scalable programmable photonics," *Opt. Lett.* **46**(22), 5671–5674 (2021).
16. R. Baghdadi et al., "Dual slot-mode NOEM phase shifter," *Opt. Express* **29**(12), 19113–19119 (2021).
17. A. Y. Takabayashi et al., "Broadband compact single-pole double-throw silicon photonic MEMS switch," *J. Microelectromech. Syst.* **30**(2), 322–329 (2021).
18. C. Errando-Herranz et al., "Low-power microelectromechanically tunable silicon photonic ring resonator add-drop filter," *Opt. Lett.* **40**(15), 3556 (2015).
19. M.-C. M. Lee and M. C. Wu, "MEMS-actuated microdisk resonators with variable power coupling ratios," *IEEE Photonics Technol. Lett.* **17**(5), 1034–1036 (2005).
20. K. Takahashi et al., "A wavelength-selective add-drop switch using silicon microring resonator with a submicron-comb electrostatic actuator," *Opt. Express* **16**(19), 14421 (2008).
21. Y. J. Park et al., "Fully reconfigurable coupled-resonator optical waveguides (CROWs) with 10 nW static power MEMS," in *Conf. Lasers and Electro-Opt.*, May, p. STh1Q.5 (2021).
22. H. Sattari et al., "Silicon photonic MEMS add-drop filter," in *Eur. Conf. Opt. Commun. (ECOC)*, December, pp. 1–4 (2020).
23. W. Bogaerts et al., "MORPHIC: programmable photonic circuits enabled by silicon photonic MEMS," *Proc. SPIE* **11285**, 1128503 (2020).
24. N. Quack et al., "MEMS-enabled silicon photonic integrated devices and circuits," *IEEE J. Quantum Electron.* **56**(1), 1–10 (2020).
25. D. J. Bell et al., "MEMS actuators and sensors: observations on their performance and selection for purpose," *J. Micromech. Microeng.* **15**(7), S153–S164 (2005).
26. P. Absil et al., "Reliable 50 Gb/s silicon photonics platform for next-generation data center optical interconnects," in *IEEE Int. Electron. Devices Meeting*, December, p. 34.2.1–34.2.4 (2017).
27. M. Pantouvaki et al., "Active components for 50 Gb/s NRZ-OOK optical interconnects in a silicon photonics platform," *J. Lightwave Technol.* **35**(4), 631–638 (2017).
28. G. Jo et al., "Wafer-level hermetically sealed silicon photonic MEMS," *Photonics Res.* **10**(2), A14–A21 (2022).
29. V. R. Almeida and M. Lipson, "Optical bistability on a silicon chip," *Opt. Lett.* **29**(20), 2387–2389 (2004).
30. G. Priem et al., "Optical bistability and pulsating behaviour in Silicon-On-Insulator ring resonator structures," *Opt. Express* **13**(23), 9623–9628 (2005).
31. H2020 MORPHIC Project - MEMS Based Zero-Power Reconfigurable Photonic Integrated Circuits, www.h2020morphic.eu.

Hamed Sattari received his PhD in photonics from the University of Tabriz, Iran, in 2014. In 2016, he joined the Q-Lab at École Polytechnique Fédérale de Lausanne (EPFL). There, he was involved in PICs projects, particularly silicon photonics to realize MEMS-based reconfigurable components. He is currently at CSEM (Swiss Center for Electronics and Microtechnology), where he is focused on developing emerging PIC platforms such as lithium niobate on insulator.

Alain Yuji Takabayashi received his PhD in microsystems and microelectronics with a focus on silicon photonic MEMS from EPFL, Switzerland, in 2021. Since then, he has been working as an R&D engineer at Enlightra, a Lausanne-based start-up developing multi-channel laser sources using frequency combs generated in optical microresonators.

Pierre Edinger received his joint MSc degree in micro and nanotechnologies for integrated systems from INPG Phelma, France, the Politecnico di Torino, Italy, and EPFL, Switzerland, in 2017. He is currently pursuing the PhD with the Department of Micro and Nanosystems, KTH Royal Institute of Technology, Stockholm, Sweden. His current research is focused on silicon photonic MEMS.

Peter Verheyen received his degree in electrical engineering and his PhD from Katholieke Universiteit Leuven, Leuven, Belgium, in 1996 and 2003, respectively. He was a doctoral researcher at the Interuniversity Microelectronics Center, Leuven, involved in advanced CMOS integration and MEMS integration. He is currently a member of the Silicon Photonics staff as a part of the 3D integration group, leading the Silicon Photonics Integration team.

Kristinn B. Gylfason received his BSc and MSc degrees in electrical engineering from the University of Iceland in 2001 and 2003, respectively, and his PhD in electrical engineering from KTH in 2010. In 2015, he received the title of Docent in micro- and nanosystems from KTH. From 2003 to 2005, he was a research engineer with Lyfjathroun Biopharmaceuticals, Iceland. He is currently an associate professor leading the team with a focus on photonic micro- and nanodevices.

Wim Bogaerts is professor in Silicon Photonics at Ghent University and IMEC, Belgium. During his PhD (2004), he developed the first silicon photonics process in a CMOS fab in IMEC. He then focused on design challenges for complex photonic circuits, eventually co-founding Luceda Photonics. Supported by a European Research Council grant, he now researches large-scale photonic circuits and programmable photonics. He is a senior member of Optica and SPIE and a fellow of IEEE.

Niels Quack is an associate professor at the University of Sydney, Australia. He received his MSc degree from Ecole Polytechnique Fédérale de Lausanne (EPFL), Switzerland, in 2005, and his DrSc degree from ETH Zürich, Switzerland, in 2010. He was a postdoc at UC Berkeley, in 2011–2015 and an assistant professor at EPFL in 2015–2021. His research focuses on Photonic Micro- and Nanosystems. He is senior member of IEEE, member of Optica, and life member of SPIE.